Anomalous crossed Andreev reflection in a mesoscopic superconducting ring hosting Majorana fermions

Minchul Lee,[1] Heunghwan Khim,[2] and Mahn-Soo Choi[2,3,*]

[1]*Department of Applied Physics, College of Applied Science, Kyung Hee University, Yongin 446-701, Korea*

[2]*Department of Physics, Korea University, Seoul 136-701, Korea*

[3]*School of Physics, Korea Institute for Advanced Study, Seoul 130-722, Korea*

(Received 7 August 2013; revised manuscript received 30 December 2013; published 17 January 2014)

We investigate the Majorana physics and its effect on the electron transport in the nontopological superconductor (NS)–topological superconductor (TS) double junctions of a loop geometry. We find that, depending on the ratio between the lengths of two topologically different regions and the localization lengths of the Majorana fermions formed between them, two completely different transport mechanisms are working: perfect crossed Andreev reflection (CAR) for the short NS segment and perfect normal Andreev reflection for the short TS segment. The difference is explained in terms of the topologically distinct properties of subgap states in two regions, which have not been revealed so far. The exotic dependence of the CAR process on the magnetic flux threading the loop is uncovered and can be used to detect the Majorana fermions.

DOI: 10.1103/PhysRevB.89.035309 PACS number(s): 73.63.Nm, 74.78.Na, 74.81.−g, 74.45.+c

I. INTRODUCTION

Solution to the Dirac equation [1,2], the first quantum theory compatible with special relativity, is complex in general, implying that to each particle there should exist an antiparticle with same mass but opposite charge. Theoretically, the Dirac equation can also have a real solution [3]. The associated particle, the so-called a Majorana fermion, must then be its own antiparticle and its charge neutral. Furthermore, Majorana fermion modes in two dimensions satisfy non-Abelian statistics, which can be explored for topologically protected quantum computation [4–6].

Whereas the Majorana fermion as an elementary particle still remains elusive with its direct observation facing formidable technical challenges, it appears to be far more abundant and experimentally accessible as an emergent quasiparticle in condensed-matter systems [7,8]. Earlier, it was shown that unpaired Majorana fermions can exist localized at the ends of p-wave superconductor wires with certain specific conditions [9], and recently several proposals have been put forward for realistic devices based on a semiconducting nanowire with strong spin-orbit coupling and in proximity to a superconductor [10–14]. Also proposed are schemes to manipulate and braid the Majorana fermions to perform quantum gates [14–16].

The zero-bias peak observed in recent experiments on InSb [17,18] and InAs [19] nanowires strongly suggests the existence of Majorana fermions. This may not be decisive evidence [20–22], though, and other evidence is worthwhile. One promising direction is to investigate the supercurrent characteristics through a Josephson junction with Majorana fermions localized at it [9,23–25].

A semiconductor nanowire with strong spin-orbit coupling and in close proximity to a superconductor turns to either a topologically nontrivial superconductor (hereafter called "topological superconductor" or TS) or a topologically trivial conventional superconductor (to be called "nontopological superconductor" or NS). With two topologically distinct superconductors at hand, one can consider three kinds of single Josephson junctions: NS-NS, TS-TS, and NS-TS junctions. The NS-NS junction is the ordinary Josephson junction in which a Cooper pair tunnels through an intermediate insulating or conducting medium [see Fig. 1(a)]. The supercurrent I in the tunneling limit is then a sinusoidal function of the phase difference $\delta\varphi \equiv \varphi_L - \varphi_R$, being periodic with a period 2π: $I = I_0 \sin\delta\varphi$. On the other hand, the TS-TS junction hosts a single fermionic excitation localized at the junction [see Fig. 1(b)]. Upon the 2π change in $\delta\varphi$, a fermionic quasiparticle is transported to the junction region and the fermion parities of the two TS regions are reversed. Another 2π change in $\delta\varphi$ restores the fermion parities. Thus the Josephson current exhibits 4π periodicity, unless there is a fermion-parity-breaking process [9,26]. For a hybrid NS-TS junction [see Fig. 1(c)], since both sides have a gap and are topologically different, a single gapless state should exist at the boundary [9,14,27]. The junction thus has a single Majorana state which is pinned at the Fermi level, irrespective of the phase difference. The supercurrent, proportional to the derivative of the Andreev bound state with respect to the phase difference [see Eq. (23)], should then be zero. The vanishing supercurrent can be argued in another way: In the Majorana state which is its own antiparticle, the particle and hole excitations have the same amplitudes. Further, since the particle and hole are at the same (Fermi) energy level, their group velocities have the same magnitude. Hence, their contributions to the current should cancel out each other exactly, and no current flows through the hybrid NS-TS junction.

Recently, Jiang *et al.* [23] proposed a way to induce a supercurrent through the hybrid NS-TS junction by making a TS-NS-TS double junction. In their setup, the middle NS is short enough that the overlap between the two Majorana states localized at both ends of the NS segment is finite. The overlap couples the two Majorana states so that their energies are lifted from the Fermi level and the vanishing current condition used above is no longer valid. They predicted two different mechanisms of electron tunneling [see Fig. 2(a)]: First, a single electron can tunnel from one TS to the other TS like in the

*choims@korea.ac.kr

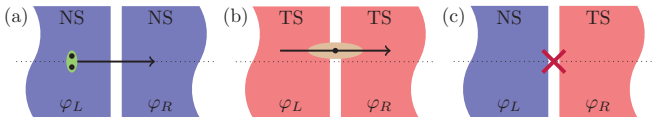

FIG. 1. (Color online) (a) NS-NS junction, with ordinary Cooper-pair (double dot in ellipse) tunneling. (b) TS-TS junction, hosting a Dirac fermion (dot in ellipse) excitation at the junction. (c) NS-TS junction, hosting a single Majorana (cross) localized at the junction. φ_L and φ_R are the superconducting phases in the left and the right superconductors.

TS-TS junction. Second, a Cooper pair in the middle NS is split, and each of the two electrons from the Cooper pair tunnels into either left or right TS. The Josephson junction energies from the two tunneling mechanisms have different dependence on the superconducting phases: the Josephson energy from the former process follows that of the TS-TS junction

$$E_M \cos\frac{\varphi_L - \varphi_R}{2}, \tag{1}$$

and the energy due to the Cooper pair splitting is given by

$$E_Z \cos\left(\frac{\varphi_L + \varphi_R}{2} - \varphi_M\right). \tag{2}$$

It was proposed to measure unusual Shapiro steps in a nonlocal ac current in order to detect the latter tunneling mechanism.

What about a NS-TS-NS double junction [see Fig. 2(b)] with a short TS segment in the middle? Interestingly, even though it is seemingly a counterpart of the TS-NS-TS double junction discussed in Ref. [23], its Majorana physics and associated supercurrent characteristics are quite different. As we will show in detail with numerically exact calculations (see Sec. III) and perturbation theory (see Appendix A), the main difference is that the energy splitting due to the overlap over the TS segment of the two Majorana states is almost independent of the phase difference and carries very little supercurrent. Putting this another way, NS-TS-NS and TS-NS-TS double junctions have topologically different characteristics: Since NS preserves the fermion parity, it cannot accept a single electron, and the two transport mechanisms working in the TS-NS-TS double junction cannot take place. In principle, the overlap between the Majorana fermions opens a fermionic channel through the short TS segment so that the Cooper pair in the NS regions can tunnel through it via virtual processes

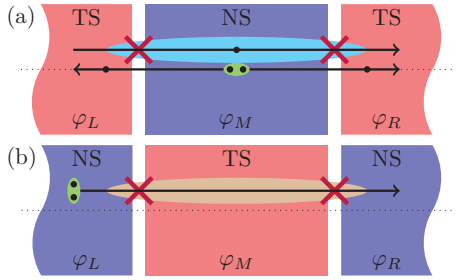

FIG. 2. (Color online) (a) TS-NS-TS double junction and (b) NS-TS-NS double junction. φ_L, φ_M, and φ_R are the superconducting phases in the left, middle, and the right superconductors.

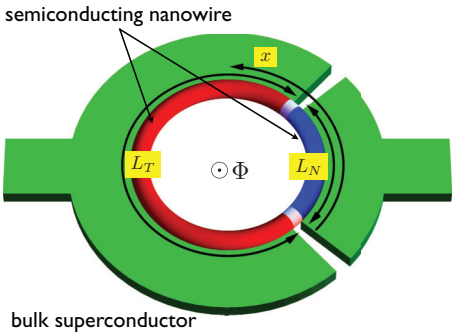

FIG. 3. (Color online) Illustration of a ring made of a semiconducting quantum wire in proximity to two s-wave superconductors. The attached superconductors are interrupted by insulators so that no current can flow directly between bulk superconductors. Different gate voltages on two segments of the quantum wire define two topologically different parts whose lengths are L_T and L_N, respectively. The external magnetic field **B** pierces the ring inducing the Zeeman splitting on the nanowire and the magnetic flux in the wire.

as depicted in Fig. 2(b). Hence, the Josephson energy in the NS-TS-NS double junction will behave like

$$E_C\left[\cos(\varphi_L - \varphi_M) + \cos(\varphi_M - \varphi_R)\right] \tag{3}$$

in a symmetric double junction. Since the Cooper pair tunneling demands the cotunneling processes, the magnitude of E_C would be significantly smaller than those of E_M and E_Z in the counterpart setup.

In this paper we investigate the Majorana physics and the corresponding electron transport in the TS-NS double junctions of a closed loop geometry as shown in Figs. 3 and 9. This setup contains both TS-NS-TS and NS-TS-NS double junction, allowing us to study them on an equal footing. The Aharonov-Bohm phase from the threading magnetic flux and the phase difference between bulk superconductors that induce the p-wave superconductivity in the nanowire control the relative phases across the junctions between NS and TS. We find that the supercurrent characteristics through the loop strongly depends on the relative ratio between the segment lengths and the localization lengths of the Majorana states. For short (compared with the localization lengths of the Majorana states) NS and long TS segments (see Section III A), the supercurrent originates solely from the crossed Andreev reflection (CAR), exhibiting an unusual dependence on the magnetic flux: the acquired magnetic phase is that by a single electron, not a Cooper pair. For short TS and long NS segments (see Section III B), on the contrary, the normal Andreev reflection (NAR) determines the supercurrent. The difference in the supercurrent features of the two extreme cases is explained in terms of topological properties in the subgap states (see Section II C). For small loops, the two mechanisms can occur simultaneously and we show that in this case the CAR process can be robust against possible fermion-parity breaking perturbations (see III C). Finally, we propose a realistic experimental setup to implement our design to detect the exotic CAR via the Majorana fermions.

The paper is organized as follows: In Section II we describe our system of p-wave superconductor double junctions of the ring geometry and the method to obtain the subgap states and

the corresponding supercurrent. In this section, we also discuss the elementary features of the subgap states and associated supercurrent of topological origin, which will provide the physical interpretations for the results to be presented in Section III. Section III presents and discusses the numerical results leaving the perturbative calculations in Section A. In Sec. IV we propose and discuss a realistic setup of our system which facilitates our predictions. Section V concludes the paper.

II. MODEL AND METHOD

A. *p*-wave superconductor junctions

We consider a narrow semiconductor ring in proximity to two spatially separated s-wave superconductors as shown in Fig. 3. The semiconductor wire forms a ring geometry with radius R and circumference $L = 2\pi R$. Here we choose a circular ring for computational convenience. However, it need not be a perfect circle as long as the nanowire forms a closed loop. Essential physics does not depend on the specific geometry. Experimental realization may prefer a closed loop with straight semiconductor segments (instead of curved segments) in favor of easier layering of nanowires and superconductors, which will be proposed in Sec. IV in details.

The attached bulk superconductors are connected to superconducting electrodes so that the supercurrent through the loop can be measured. In the loop part, two (lower and upper) junctions at $x = x_a = 0$ and $x = x_b = L_N$ are introduced by inserting insulating regions between superconductors. Here x denotes the position coordinate along the circumference (see Fig. 3). Here we assume that the insulators are thick enough so that no current can flow directly between superconductors. However, since the supercurrent can still flow between two superconductors through the nanowire, the relative phase of the superconducting order parameter, $\varphi(x)$, between two superconductors can be defined. First, a bias current applied across the loop induces a phase difference as

$$\varphi_0(x) = \begin{cases} \varphi_N & (x_a < x < x_b), \\ \varphi_T & (x_b < x < L). \end{cases} \tag{4}$$

In addition, in the presence of the magnetic flux Φ threading the loop, the superconducting phase depends on the position and in a proper gauge is given by $\varphi(x) = 4\pi f x/L$ [from the vanishing-current condition inside the superconductors, $0 = \hbar\partial_x\varphi(x) - 2eA_x$ with the azimuthal component A_x of the vector potential], where $f \equiv \Phi/\Phi_0$ is the dimensionless magnetic flux and $\Phi_0 \equiv h/e$ is the flux quantum for a *single* electron. Putting them all together, the superconducting phase takes the form

$$\varphi(x) = \varphi_0(x) + 4\pi f\frac{x}{L}, \tag{5}$$

resulting in finite phase differences at two junctions:

$$\delta\varphi|_{x=x_a} = 4\pi f - \delta\varphi, \quad \delta\varphi|_{x=x_b} = \delta\varphi \tag{6}$$

with $\delta\varphi \equiv \varphi_T - \varphi_N$. Via the proximity effect, the bulk superconductors induce an s-wave superconductivity on the semiconducting nanowire, on which the order parameter is given by $\Delta(x) = \Delta_0 e^{i\varphi(x)}$.

Assuming that the semiconducting nanowire is narrow enough that only the lowest transverse mode is involved, the Hamiltonian of the superconductivity-induced wire then reads

$$H = \oint dx \left\{ [\psi_\uparrow^\dagger(x) \quad \psi_\downarrow^\dagger(x)] \left(\frac{\Pi_x^2}{2m} - \mu_F(x) + \frac{V_Z}{2}\sigma_z + \frac{\alpha}{\hbar}\frac{\{\boldsymbol{\sigma}\cdot\mathbf{u}(x), \Pi_x\}}{2} \right) \begin{bmatrix} \psi_\uparrow(x) \\ \psi_\downarrow(x) \end{bmatrix} + \Delta(x)\psi_\uparrow^\dagger(x)\psi_\downarrow^\dagger(x) + (\text{H.c.}) \right\} \tag{7}$$

with $\Pi_x = p_x - 2\pi\hbar f/L$. The field operator $\psi_s(x)$ describes the electronic degrees of freedom in the lowest transverse mode with spin $s = \uparrow,\downarrow$ and effective mass m ($m \approx 0.015m_e$ for InSb [17,18] and $m \approx 0.03m_e$ for InAs [19]).

One of the key ingredient for effective p-wave superconductivity is the strong Rashba spin-orbit coupling, which is specified by the parameter α ($\alpha \approx 0.2$ eV Å for InSb [17,18] and InAs [19]) or equivalently by the spin-orbit length $\ell_{so} \equiv \hbar^2/m\alpha$ ($\ell_{so} \approx 200$ nm for InSb [17,18] and $\ell_{so} \approx 127$ nm for InAs [19]). The Rashba-induced effective magnetic field, assumed to lie in the ring plane, is perpendicular to the wire direction and hence varies along the wire, and $\mathbf{u}(x) = \hat{\mathbf{x}}_1\cos\phi(x) + \hat{\mathbf{x}}_2\sin\phi(x)$ is the unit vector parallel to the Rashba field at the position x (here $\hat{\mathbf{x}}_1$ and $\hat{\mathbf{x}}_2$ are the unit vectors in the ring plane of the laboratory frame). The inner curly brackets denote the anticommutator, and guarantee the hermiticity of H in the presence of position-dependent Rashba field $\mathbf{u}(x)$.

The other ingredient is the Zeeman field V_Z perpendicular to the Rashba field, which is assumed to be applied perpendicular to the ring plane. The applied magnetic field should induce a finite spin splitting but be still weak enough not to break the superconductivity ($B \sim 100$ mT [17,18]). The shielding of the perpendicular magnetic field by the underlying superconductors can be avoided by letting the superconductor cover the nanowire only partially as done in a recent experiment [17]. We will discuss this matter in more detail in Sec. IV.

Finally, $\mu_F(x)$ is the position-dependent chemical potential, with $\mu_F(x) = \mu_N$ for $x_a < x < x_b$ and μ_T for $x_b < x < L$. As will be discussed below, the topological state of each region is controlled by locally tuning the chemical potential.

The model Eq. (7) for a uniform wire (closed or open) is exactly solvable via the Bogoliubov–de Gennes (BdG) transformation in the chiral basis diagonalizing the single-particle part of the Hamiltonian [27]. The two channels with chirality $\zeta = \pm$ (representing two spin directions with respect to the momentum direction) are completely decoupled and a finite p-wave pairing potential between electrons with same spin in each channel is induced, whose order parameter is proportional to $\alpha\Delta_0/V_Z$ in the small momentum limit. It illustrates that the Rashba spin-orbit coupling, the Zeeman splitting, and the s-wave superconductivity combines together to form three indispensable ingredients to implement the p-wave superconductor. Even though both channels exhibit the p-wave superconductivity, the excitation gap between particle and hole bands in one of them (say $\zeta = +$) remains finite at

any value of momentum k, irrespective of the strength of the system parameters. On the other hand, the gap for the other channel ($\zeta = -$) can close when the parameters are properly tuned. Hence, near the quantum phase transition point, only the $\zeta = -$ channel is relevant and one can project out the other channel by focusing on the low-energy physics. The projection onto the $\zeta = -$ channel then gives rise to an effective p-wave superconducting wire of spinless fermions:

$$H_{\rm eff} = \oint dx \left[\psi^\dagger(x) \left(\frac{\Pi_x^2}{2m_{\rm eff}} - \mu_{\rm eff}(x) \right) \psi(x) + \frac{\Delta_{\rm eff}(x)}{2} \psi^\dagger(x) \partial_x \psi^\dagger(x) + ({\rm H.c.}) \right] \tag{8}$$

with the effective mass $m_{\rm eff} = (1/m - \alpha^2/\hbar^2 V_Z)^{-1}$ and the effective chemical potential $\mu_{\rm eff}(x) = \mu_F(x) + V_Z - \Delta_0^2/2V_Z$. The induced p-wave order parameter

$$\Delta_{\rm eff}(x) = \frac{\alpha \Delta_0}{\hbar V_Z} i e^{i[\varphi(x)+\phi(x)]} \tag{9}$$

has two contributions to its phase: $\varphi(x)$ inherited from the phase of the order parameter of the bulk superconductors, and $\phi(x)$ from the position-dependent direction $\mathbf{u}(x)$ of the Rashba field. The corresponding BdG equation has the form

$$i\hbar \frac{\partial}{\partial t} \begin{bmatrix} \psi(x) \\ \psi^\dagger(x) \end{bmatrix} = H_{\rm eff}^{\rm BdG} \begin{bmatrix} \psi(x) \\ \psi^\dagger(x) \end{bmatrix} \tag{10}$$

with

$$H_{\rm eff}^{\rm BdG} = \begin{bmatrix} \frac{(p_x - 2\pi\hbar f/L)^2}{2m_{\rm eff}} - \mu_{\rm eff}(x) & \frac{1}{2}\{\Delta_{\rm eff}(x), p_x\} \\ \frac{1}{2}\{\Delta_{\rm eff}^*(x), p_x\} & -\frac{(p_x + 2\pi\hbar f/L)^2}{2m_{\rm eff}} + \mu_{\rm eff}(x) \end{bmatrix}. \tag{11}$$

Below we solve the effective model, Eqs. (8), (10), and (11), by first seeking the solution for each uniform wire segment and then matching the solutions across the junctions.

B. Bulk states in a uniform segment

For a uniform wire segment with $\mu_{\rm eff}$ and $\Delta_{\rm eff}$ constant, the bulk spectrum for a particle-like (E_+) and hole-like (E_-) excitation are given by

$$E_\pm(\tilde{k}) = E_R(\tilde{k} \pm \sqrt{(\tilde{k}^2 - \tilde{\mu})^2 + \tilde{\Delta}^2 \tilde{k}^2}), \tag{12}$$

with

$$\tilde{k} \equiv kR, \quad E_R \equiv \frac{\hbar^2}{2m_{\rm eff}R^2}, \quad \tilde{\mu} \equiv \frac{\mu_{\rm eff}}{E_R} - \frac{1}{4}, \quad \tilde{\Delta} \equiv \frac{\hbar|\Delta_{\rm eff}|}{E_R R} = \frac{2\Delta_0}{V_Z}\frac{R}{\ell_{so}}. \tag{13}$$

The spectrum becomes gapless for $\tilde{\mu} = 0$, at which occurs the topological phase transition between a topological phase (T) with $\tilde{\mu} > 0$ and a nontopological phase (N) with $\tilde{\mu} < 0$.

The spectrum is asymmetric with respect to $\tilde{k} \to -\tilde{k}$; see Fig. 4. The variation of the Rashba field direction along the curved wire invokes the precession of electron spin, and the resulting Berry phase leads to a finite z component in the spin polarization axis which is exactly opposite for clockwise ($\tilde{k} < 0$) and counterclockwise ($\tilde{k} > 0$) movers. Adding the Zeeman field, therefore, makes the magnitude of the z component different for two opposite movers, introducing asymmetry between them [28]. As a result, the gap between the particle and hole bands is indirect. In particular, for small $\tilde{\Delta} < 1$, the system is metallic over the whole range of energy; see Fig. 4(a). However, such an asymmetry effect is pronounced only for a very small loop ($R \ll \ell_{so} V_Z/2\Delta_0 \approx 200$ nm). In our study, we therefore focus on the case with $\tilde{\Delta} > 1$, where the gap $E_{\rm gap}$ is finite and almost direct [see Fig. 4(b)].

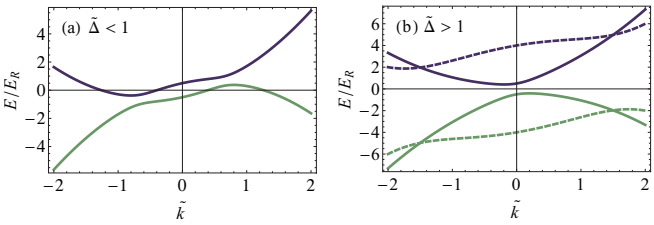

FIG. 4. (Color online) Bulk spectrum for the uniform chemical potential and superconducting phase, Eq. (12), for p-wave superconducting wire of ring geometry for (a) $\tilde{\Delta} < 1$ and (b) $\tilde{\Delta} > 1$. The case (a) is achievable only for very small rings and we focus on the case (b) in this work. In (b), the solid and dashed lines correspond to the bulk spectrum in the topological phase with $\tilde{\mu} < D \equiv (\tilde{\Delta}^2 - 1)/4$ and $\tilde{\mu} > D$, respectively.

The bulk eigenstates corresponding to the spectrum, Eq. (12), are

$$\chi_{k,+}(x) = e^{ikx} \begin{bmatrix} e^{+i(\varphi/2 + (f+1/2)x/R)} \cos\frac{\vartheta_k}{2} \\ e^{-i(\varphi/2 + (f+1/2)x/R)} \sin\frac{\vartheta_k}{2} \end{bmatrix}, \tag{14a}$$

$$\chi_{k,-}(x) = e^{ikx} \begin{bmatrix} -e^{+i(\varphi/2 + (f+1/2)x/R)} \sin\frac{\vartheta_k}{2} \\ e^{-i(\varphi/2 + (f+1/2)x/R)} \cos\frac{\vartheta_k}{2} \end{bmatrix}, \tag{14b}$$

with the angle ϑ_k defined by $\tan\vartheta_k = \tilde{\Delta}\tilde{k}/(\tilde{k}^2 - \tilde{\mu})$. The phase $\pm x/2R$ in the exponents originates from the variation of the Rashba field direction, $\phi(x)$, resulting in the Berry phase π for one cycle along the loop. As can be seen from Eq. (14), this Rashba phase always appears together with the magnetic flux f in the form of $f + 1/2$. In other words, the actual effect of the Rashba phase is to apply an additional half flux quantum $\Phi_0/2$ through the loop.

C. Topological property of subgap states at junctions

By applying a nonuniform chemical potential along the loop as given by

$$\tilde{\mu}_{\rm eff}(x) = \begin{cases} \tilde{\mu}_N < 0 & (x_a < x < x_b), \\ \tilde{\mu}_T > 0 & (x_b < x < L), \end{cases} \tag{15}$$

the two segments become topologically different superconductors, and a localized Majorana state is formed at each interface $x = x_{a,b}$ [9,14]. Before obtaining exact subgap states in the nonuniform configuration (see Sec. II D), we examine the topological structure of the Majorana states localized at the junctions. Here we focus on the case of isolated Majorana states and disregard the interaction between them. For further simplicity, we turn off the magnetic flux ($f = 0$). Without the interaction, the energy of the Majorana state is zero, and by seeking zero-energy solution in Eqs. (12) and (14) for $\tilde{\mu}_T < D$,

we obtain four purely imaginary wave vectors

$$k_{\eta\nu}^{\ell} = \eta i/\lambda_{\ell\nu} \tag{16}$$

and the corresponding wave functions

$$\chi_{\eta,\nu}^{\ell}(x) = e^{ik_{\eta\nu}^{\ell}x}\begin{bmatrix} e^{+i(\varphi_\ell/2+x/2R)}e^{+i\gamma_{\eta\nu}^{\ell}/2} \\ e^{-i(\varphi_\ell/2+x/2R)}e^{-i\gamma_{\eta\nu}^{\ell}/2} \end{bmatrix} \tag{17}$$

for each region $\ell = T,N$. Here $D \equiv (\tilde{\Delta}^2 - 1)/4$, $\nu = 1,2$ distinguishes different Majorana modes with different localization lengths ($\lambda_{\ell 1} \geqslant \lambda_{\ell 2}$), and the index $\eta = \pm$ denotes the decay direction of the wave function tail: $\eta = +(-)$ state decays in the positive (negative) direction. Note that while the wave vectors $k_{\eta\mu}^{N}$ in the NS region are always purely imaginary no matter what values $\tilde{\mu}_N < 0$ has, the wave vectors $k_{\eta\mu}^{T}$ in the TS region can have real parts if it is in deep topological phase ($\tilde{\mu}_T > D$) [see Fig. 4(b)]. However, since the finite real parts do not affect the topological features which are our main concern, we focus on the $\tilde{\mu}_T < D$ case, and the $\tilde{\mu}_T > D$ case will be separately discussed in Appendix C.

The imaginary parts of the wave vectors $k_{\eta\nu}^{\ell}$ determine the localization length of the Majorana states. In the NS region ($\tilde{\mu}_N < 0$) and the TS region ($0 < \tilde{\mu}_T < D$), the localization lengths are given by

$$\lambda_{N\nu} = \frac{R}{\sqrt{D+|\tilde{\mu}_N|}+(-1)^{\nu}\sqrt{D}}, \tag{18a}$$

$$\lambda_{T\nu} = \frac{R}{\sqrt{D}+(-1)^{\nu}\sqrt{D-\tilde{\mu}_T}}, \tag{18b}$$

respectively. The relative phase difference $\gamma_{\eta\nu}^{N} = \eta(-1)^{\nu}\gamma$ in the NS region depends on both η and ν, where the angle γ has been defined by

$$e^{i\gamma} \equiv -\frac{1}{\tilde{\Delta}} + i\sqrt{1-\frac{1}{\tilde{\Delta}^2}}, \tag{19}$$

but $\gamma_{\eta\nu}^{T} = \eta\gamma$ in the TS region does not depend on ν. This difference leads to intriguing topological properties as we discuss below. The wave functions $\Psi_i(x)$ for Majorana states localized at $x = x_i$ ($i = a,b$) are then given by linear superpositions of the eigenstates, Eq. (17); refer their explicit forms to Eq. (A1). The coefficients for eigenstates are determined by the matching condition at each junction:

$$\Psi_i(x_i^+) = \Psi_i(x_i^-), \quad v_x\Psi_i(x_i^+) = v_x\Psi_i(x_i^-), \tag{20}$$

where v_x is the velocity operator along the wire

$$v_x = \begin{bmatrix} -iR\partial_x - f & \frac{\tilde{\Delta}}{2}e^{+i[\varphi(x)+(2f+1)\frac{x}{R}]} \\ \frac{\tilde{\Delta}}{2}e^{-i[\varphi(x)+(2f+1)\frac{x}{R}]} & iR\partial_x - f \end{bmatrix}. \tag{21}$$

Note that $x_a^- = L$.

In order to clarify the topological difference between the wave functions, Eq. (17), of the NS and TS regions, we regard the wave functions as spinors in the pseudospin up ($\uparrow$) and down ($\downarrow$) basis in the particle-hole (or so-called Nambu) space, and examine their pseudospin polarization directions. Figure 5 shows the pseudospin polarization of the eigenstates localized at the TS-NS and NS-TS junctions for $\delta\varphi = 0$. We see the clear difference between relative pseudospin polarizations in

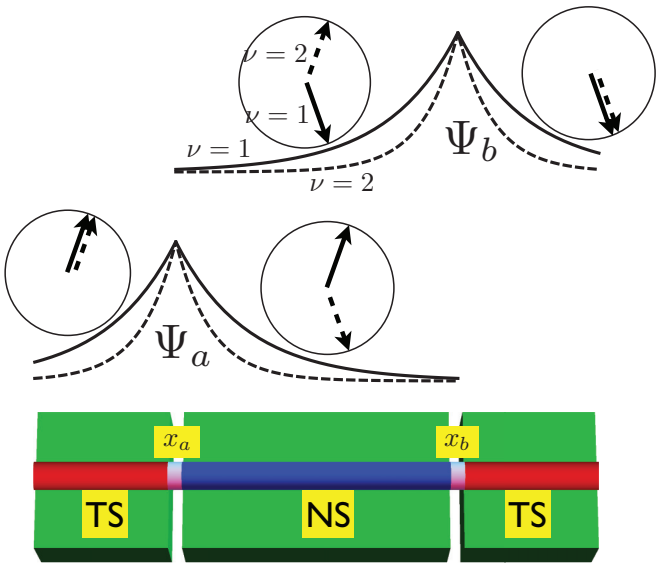

FIG. 5. (Color online) A schematic representation of the subgap states, Ψ_a and Ψ_b, at the TS-NS (x_a) and NS-TS (x_b) junction interface, respectively. The curves depict the spatial distributions of the wave functions, and the arrows in circles the pseudospin polarizations in the particle-hole basis. The solid and dotted curves/arrows correspond to $\nu = 1$ and 2 Majorana mode, respectively. Here no superconducting phase difference ($\delta\varphi = 0$) is applied for simplicity. Note that for finite length of the NS segment, the wave function Ψ_a should be matched with Ψ_b properly at $x = x_b$, and Ψ_b with Ψ_a at $x = x_a$. When matching, the $\nu = 1$ mode undergoes a pseudospin rotation by angle 2γ, while the $\nu = 2$ mode does not.

two topologically different regions. In the NS region, the two evanescent modes ($\nu = 1,2$) localized at the same end form an angle 2γ ($\pi/2 < \gamma < \pi$), while they are parallel to each other in the TS region: For an infinite-curvature ring ($\tilde{\Delta} \gg 1$), $\gamma \approx \pi/2$ so the two modes are polarized in the opposite direction. The phase difference $\delta\varphi = \varphi_N - \varphi_T$ leads to the misalignment between the polarization axes for the two regions [31].

This topological difference leads to two important consequences which are experimentally detectable. First, the overlap between Majorana fermions has different nature according to whether they are coupled through the NS or the TS regions. For example, in the TS region, the pseudospins of two modes are always aligned and rotate in the same way so they are always in phase, which is the main reason why the overlap of Majorana states through the TS region is almost a constant independent of phases. On the other hand, the two modes in the NS region are not aligned so that their amplitudes depend on the superconducting phases and the magnetic flux. In Sec. III, we will see a stark contrast in the properties of the supercurrents in the two cases.

Second, the two modes acquire different phases while they travel through the NS region; see Fig. 5. While the $\nu = 1$ mode in the left TS region tunnels to the NS region without a rotation, it has to rotate by 2γ to match with the $\nu = 1$ mode in the right TS region. This rotation should be reflected in the overlap matrix element between Ψ_a and Ψ_b. However, the $\nu = 2$ mode rotates in the left TS-NS junction, while it is then already aligned with the $\nu = 2$ mode in the right TS region. The

pseudospin rotation at the left junction just contributes to an overall phase of Ψ_a so that it does not affect the Ψ_a-Ψ_b overlap matrix element. Hence, the phase difference 2γ between two modes arises. Note that this additional phase does not take place in the case of the crossed Andreev reflection (Cooper pair splitting) where two electrons in the middle NS region go in the opposite directions. In this case the pseudospin rotates in the opposite directions for opposite-moving electrons so that the phases are canceled out. Hence, this pseudospin rotation in the particle-hole space severely affects the relative amplitudes of currents due to the single-electron tunneling and the crossed Andreev reflection through the TS-NS-TS junctions, which will be discussed in Sec. III A.

D. Subgap states and supercurrent in a closed ring

Now we examine the effects of the finite size of the segments between the junctions and the closed-loop geometry (periodic boundary condition); see Fig. 3. For finite-size segments between two junctions, the wave functions of two localized Majorana modes have a finite overlap, which gives rise to finite energies $\pm E_A$ of subgap eigenstates with $|E_A| \leqslant E_{\rm gap} = \min(E^T_{\rm gap}, E^N_{\rm gap})$ where $E^\ell_{\rm gap}$ is the gap in each region ($\ell = T, N$). The overlap E_A depends exponentially on the ratio of the segment length L_ℓ ($\ell = N, T$) to the localization lengths $\lambda_{\ell\nu}$ of the Majorana states. The effective low-energy Hamiltonian can be then written as

$$H_M = E_A(2d^\dagger d - 1), \tag{22}$$

where $d = (\gamma_a + i\gamma_b)/\sqrt{2}$ is the fermionic operator from the Majorana fermion operators $\gamma_{a,b}$. The subgap eigenstates are then labeled as $|0\rangle$ and $|1\rangle \equiv d^\dagger|0\rangle$. The supercurrent corresponding to the eigenstate is then calculated by taking the derivative of the energy [32]:

$$I = \frac{2e}{\hbar}\frac{\partial H_M}{\partial \delta\varphi}. \tag{23}$$

We determine the exact subgap energy E_A by solving the BdG equation, Eq. (10) in each region and matching the solutions across the interfaces at $x = x_a$ and x_b imposing the boundary conditions analogous to Eq. (20). Explicitly, one has to solve self-consistently $E_A = E_+(\tilde{k})$ [$E_A = E_-(\tilde{k})$ gives identical results due to the particle-hole symmetry] and the boundary condition

$$\Psi(x_i^+) = \Psi(x_i^-), \quad v_x\Psi(x_i^+) = v_x\Psi(x_i^-) \tag{24}$$

for $i = a, b$ and

$$\Psi(x) = \sum_{\eta\nu}\begin{cases} c^N_{\eta\nu}\chi^N_{k^N_{\eta\nu},+}(x) & (x_a < x < x_b), \\ c^T_{\eta\nu}\chi^T_{k^T_{\eta\nu},+}(x) & (x_b < x < L). \end{cases} \tag{25}$$

Here $k^\ell_{\eta\nu}$ are four solutions of $E_A = E_+(\tilde{k})$ with $\tilde{\mu} = \tilde{\mu}_\ell$ and $c^\ell_{\eta\nu}$ the coefficient for each mode. In the following section, the self-consistent equations are numerically solved to obtain and examine the energy E_A as a function of the magnetic flux f and the phase difference $\delta\varphi$ for given parameters.

III. RESULTS AND DISCUSSIONS

In this section we present the subgap eigenenergy E_A and the supercurrent I by using the method described in Sec. II. First, we consider two extreme cases where either the NS (Sec. III A) or TS (Sec. III B) segment is short compared with the localization lengths of the Majorana states, and show that the two cases exhibit distinct behaviors in subgap energy and supercurrent. Next, we study the small-loop case (Sec. III C) where both the behaviors are expected to arise simultaneously.

Throughout the section, we choose $R \approx 300$ nm, $m \approx 0.015m_e$ (m_e is the bare electron mass), $\alpha \approx 2 \times 10^{-11}$ eV m, and $\Delta_0 \approx V_Z \approx 300$ μeV, which are suitable for realistic samples. They correspond to $E_R \approx 20$ μeV and $\tilde{\Delta} \approx 3$ in the effective model. The value of $\tilde{\mu}_\ell$ can be varied by the gate voltage.

A. Short NS segment ($L_N \sim \lambda_{N1}$, $L_T \gg \lambda_{T1}$)

First, we consider the case in which the NS segment is short and the TS segment is very long: $L_N \sim \lambda_{N1}$ and $L_T \gg \lambda_{T1}$. Figures 6(a)–6(c) present our numerical results for the subgap eigenenergy E_A as a function of $\delta\varphi$ and f. We find that these results fit well to the expression

$$E_A \approx E_M\cos(2\pi f + \gamma_M) + E_Z\cos(\delta\varphi - 2\pi f + \gamma_Z). \tag{26}$$

Figures 6(b) and 6(c) show that for $L_N \gtrsim \lambda_{N1}$, the coefficients (E_M and E_Z) and the phase shifts ($\gamma_M \approx \pi - 2\gamma$ and $\gamma_Z \approx 0$; refer detailed analysis to Appendix B) are in a good agreement with the perturbative results (dashed line) calculated in Appendix A. For a large loop ($\tilde{\Delta} \gg 1$) with a short NS segment ($L_N \sim \lambda_{N1}$), the perturbation theory suggests a simpler expression of the coefficients and the phase shifts: $\gamma_M \approx \gamma_Z \approx 0$ and

$$E_M \approx E_R\frac{\epsilon_1}{N_0}(e^{-L_N/\lambda_{N1}} + e^{-L_N/\lambda_{N2}}), \tag{27a}$$

$$E_Z \approx E_R\frac{\epsilon_1}{N_0}(e^{-L_N/\lambda_{N1}} - e^{-L_N/\lambda_{N2}}). \tag{27b}$$

Refer the definitions of ϵ_1 and N_0 to Eqs. (A13) and (A17).

The subgap expression Eq. (26) is consistent with that of Jiang *et al.* [23] [see Eqs. (1) and (2)]. To see this, substitute the superconducting phases as follows:

$$\varphi_L \to \varphi_T, \quad \varphi_M \to \varphi_N, \quad \varphi_R \to \varphi_T + 4\pi(f + 1/2). \tag{28}$$

Note that the phase shift $4\pi(f + 1/2)$ in φ_R is the phase acquired by a Cooper pair circling around the loop in the presence of the magnetic flux and the Rashba field. Then, the single-electron tunneling term becomes

$$E_M^{\rm Jiang}\cos\frac{\varphi_L - \varphi_R}{2} \to -E_M^{\rm Jiang}\cos 2\pi f \tag{29}$$

corresponding to the E_M term in Eq. (26), and the Cooper pair splitting term becomes

$$E_Z^{\rm Jiang}\cos\left(\frac{\varphi_L + \varphi_R}{2} - \varphi_M\right) \to -E_Z^{\rm Jiang}\cos(\delta\varphi - 2\pi f) \tag{30}$$

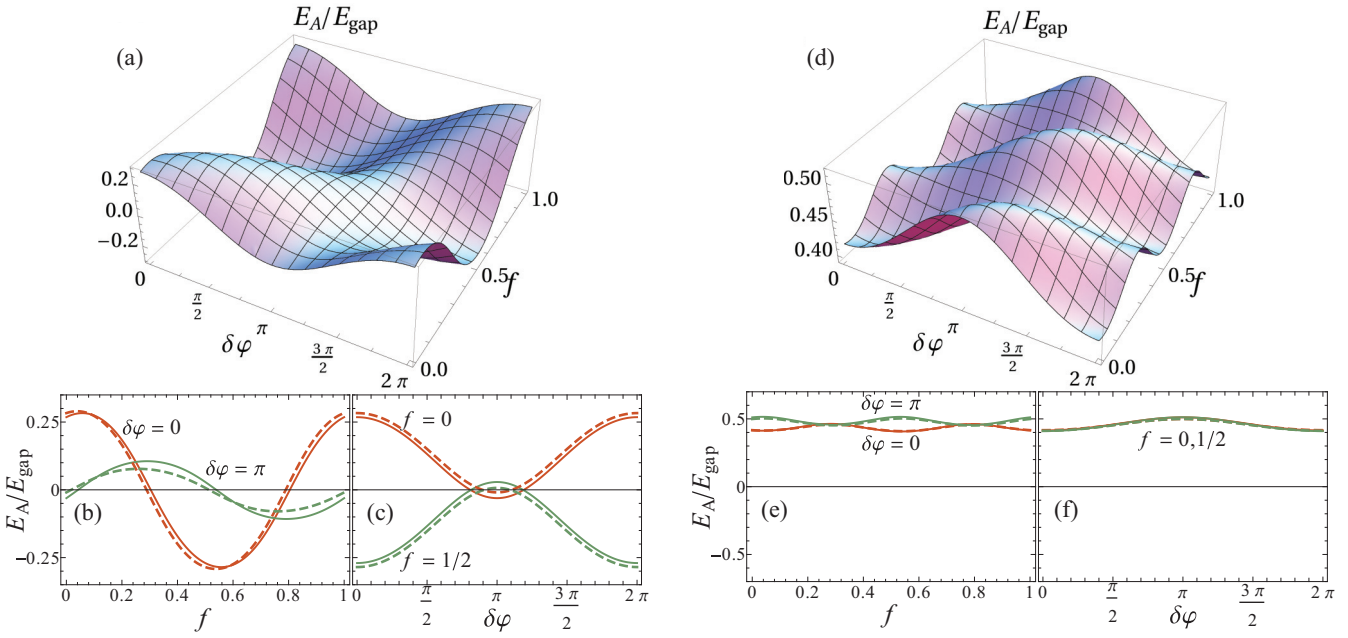

FIG. 6. (Color online) Subgap energy for the state $|1\rangle$ as a function of [(a), (d)] $\delta\varphi$ and f, [(b), (e)] f for fixed values of $\delta\varphi$, and [(c), (f)] $\delta\varphi$ for fixed values of f for [(a), (b), (c)] a loop with short NS and long TS segments, $L_N/\lambda_{N1} \approx 1.55$ and $L_T/\lambda_{T1} \approx 7.11$, and [(d), (e), (f)] a loop with long NS and short TS segments, $L_N/\lambda_{N1} \approx 6.35$ and $L_T/\lambda_{T1} \approx 1.60$. Solid and dashed lines in (b), (c), (e), and (f) correspond to the exact and perturbative energies, respectively. Here we have used $\tilde{\Delta} = 3$, $\tilde{\mu}_N = -5$, $\tilde{\mu}_T = 3$, and $E_{\rm gap} \approx 53\ \mu$eV.

corresponding to the E_Z term in Eq. (26). The sign change is ascribed to the Rashba phase which adds additional phase π upon circling around the loop.

The E_M term comes from the circulation of a single electron around the loop. In fact, the phase $2\pi f$ is exactly the magnetic phase acquired by a single electron enclosing the magnetic flux f. The additional phase γ_M arises due to the finite curvature of the loop, as discussed in Sec. II B and Appendix B. The contributions from $\nu = 1,2$ modes to the E_M term are simply additive. As discussed in Sec. II C, the $\nu = 1$ mode acquires the phase $2\gamma \approx \pi$ with respect to the $\nu = 2$ mode, which leads to a sign difference between them. On the other hand, the diagonal component of the velocity operator in Eq. (21) suggests that the supercurrent measures the pseudospin current. Since the pseudospins of the two modes in the NS segment are nearly opposite to each other (since $\gamma \approx \pi/2$), their contribution to the supercurrent is opposite in sign. Hence, gathering two sign changes, there is no sign difference between the two modes.

The E_Z term is due to the Cooper pair tunneling between TS and NS segments, accompanying the splitting of the Cooper pair. Each of two electrons in a Cooper pair tunnels between two segments through either of two TS-NS boundaries, respectively. In other words, the crossed Andreev reflection takes place with no normal Andreev reflection accompanied. This perfect CAR is due to the interesting characteristic of the TS-NS junction as discussed in Sec. I: no Cooper pair can tunnel directly across a single TS-NS junction.

Here three remarks are worthwhile concerning the CAR process involved in the E_Z term. (i) As seen in Eqs. (26) and (30), the CAR process acquires the phase $\delta\varphi - 2\pi f$. The phase $\delta\varphi$ is obviously due to the tunneling of a Cooper pair between two different superconductors. The appearance of the phase $2\pi f$ is interesting because it is identical to that by the circulation of a single electron. It indicates that the splitting and the recombination of the Cooper pair should take place at the same TS-NS boundary so that only one of two electrons split moves around the loop before the recombination, resulting in the phase $2\pi f$. The recombined Cooper pair at one of the boundaries then flows into the bulk superconductor, not being affected by the magnetic flux any more. This is consistent with the fact that the Majorana fermions are localized at the boundaries. This dependence on the magnetic flux is the evidence that the CAR is realized via the Majorana fermions.

(ii) Unlike in the E_M term above, no extra pseudospin rotation between two modes (see Sec. II C) accompanying tunneling across NS-TS junctions takes place, while the pseudospin currents of the two modes are opposite in sign. Hence, Eq. (27b) exhibits the negative combination between two modes.

(iii) As a consequence of the effect (ii), the E_Z term depends nonmonotonically on the length L_N of the NS segment, while the E_M term exhibits monotonic behavior, as shown in Fig. 7. The exponential factors $e^{-L_N/\lambda_{N\nu}}$ in both the E_M and E_Z terms imply that the finite overlap between Majorana fermions is indispensable to observe these processes. It is also known that the CAR process can happen substantially only over lengths shorter than the size of the Cooper pair (i.e., the superconducting coherence length). Based on both, one may naively expect that the CAR process (and hence E_Z) gets stronger with decreasing L_N. However, the tunneling processes through two modes $\nu = 1,2$ give opposite contributions as shown in the above (ii), due to the topological characteristic of the subgap

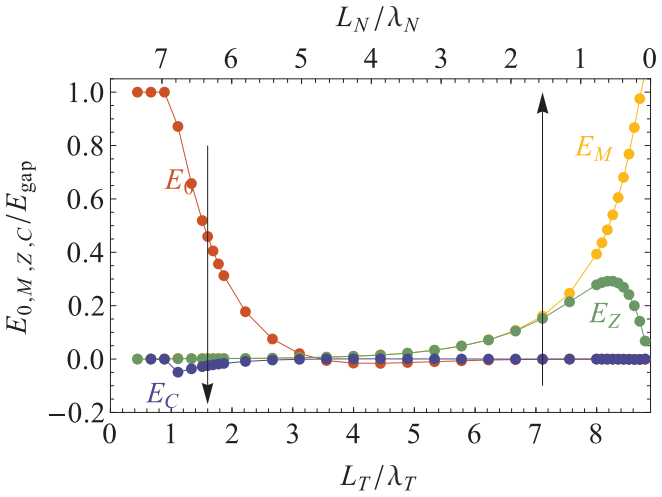

FIG. 7. (Color online) The coefficients E_M, E_Z, E_0, and E_C as functions of L_N or $L_T = L - L_N$ with $L = L_N + L_T$ fixed. The arrows indicate the segment lengths L_N and L_T with which the short-NS-segment case [Figs. 6(a)–6(c)] and the short-TS-segment case [Figs. 6(d)–6(f)] are studied. Here we have used $\tilde{\Delta} = 3$, $\tilde{\mu}_N = -5$, and $\tilde{\mu}_T = 3$.

states. Therefore the CAR process becomes weaker if the NS segment is too small: E_Z increases as L_N decreases until $L_N \geqslant \lambda_{N2}$, but decreases with decreasing L_N smaller than λ_{N2} ($\leqslant \lambda_{N1}$). On the other hand, the E_M term, due to the circulation of a single electron, increases monotonically with decreasing L_N, approaching the energy gap $E_{\rm gap}$ as $L_N \to 0$. In this limit, the Majorana fermions are strongly bound so that they become completely fermionic.

Since in both the E_M and E_Z terms it is a single electron, not a Cooper pair, that circulates around the loop, the periodicity of the subgap energy E_A with respect to the magnetic flux f is 1, not 1/2 as in the normal superconductor loop, which is clearly revealed in Fig. 6(b). The $f = 1$ periodicity is protected as long as no fermion-parity breaking mechanism is introduced into the system; if the parity breaking were present, the periodicity would be reduced to 1/2.

Now we compute the corresponding supercurrent through the loop by combining Eqs. (22), (23), and (26). The supercurrent is obtained as [33]

$$I \approx (2d^\dagger d - 1)\frac{2e}{\hbar} E_Z \sin(\delta\varphi - 2\pi f). \tag{31}$$

As a matter of fact, only the E_Z term contributes to the supercurrent: the E_M term does not involve the transport of the Cooper pair. The current also exhibits the $f = 1$ periodicity, which is the fingerprint of the Majorana fermions. If one introduces parity-breaking mechanisms into our system, the $f = 1$ periodicity may fade away. While the finite gap in the normal superconductor protects the fermion parity at sufficiently low energies, the fermion parity in the topological superconductor can be changed via Majorana fermions. For example, the electron leakage from the TS region to a gapless metal can lead to the coupling between $|0\rangle$ and $|1\rangle$ states, resulting in the anticrossing between them and restoring $f = 1/2$ periodicity. However, one can still detect the existence of the Majorana fermion by examining the response of the supercurrent with respect to the variation of both $\delta\varphi$ and f. In the following section, we will compare the supercurrents due to the crossed and normal Andreev reflections and discuss how to distinguish between them. One thing to be noted here is that in the CAR process the role of the magnetic flux f is shifting the current by $2\pi f$ without modulating the amplitude of the current.

Finally, we would like to note that all the properties of the subgap energy and the supercurrent are independent of the length of the TS segment as long as it is sufficiently larger than the size of the Majorana fermions. This is in contrast to the high dependence of the E_Z term on the relative length between the NS segment length and the Cooper pair size. This indicates that the Majorana fermion state in the TS region is highly nonlocal. In other words, this L_T independence reflects that the correlation length and the size of the Cooper pair in the TS are almost infinite as long as the coherence is preserved.

B. Short TS region ($L_N \gg \lambda_{N1}$, $L_T \sim \lambda_{T1}$)

Now we consider the opposite case in which the TS segment is short and the NS segment long: $L_T \sim \lambda_{T1}$ and $L_N \gg \lambda_{N1}$. Interestingly, in this case the physics of the Majorana fermions is completely different compared to the former case, as shown in Figs. 6(d)–6(f). In this regime, we obtain the following empirical expression for the subgap energy:

$$E_A \approx E_0 + E_C\left[\cos\delta\varphi + \cos(4\pi f - \delta\varphi)\right]. \tag{32}$$

Figures 6(e) and 6(f) show that our exact and perturbative results match well with each other. The simpler expressions for the coefficients E_0 and E_C are at hand in the large-loop limit and for $L_T/\lambda_{T1} \gtrsim 1$:

$$E_0 \approx \frac{E_R}{N_0}[(\epsilon_1 + \epsilon_2)e^{-L_T/\lambda_{T1}} + (\epsilon_1 - \epsilon_2)e^{-L_T/\lambda_{T2}}], \tag{33a}$$

$$E_C \approx \frac{\sqrt{D}}{2\tilde{\mu}_N N_0} E_0. \tag{33b}$$

See Eqs. (A13) and (A17) for the definition of $\epsilon_{1,2}$ and N_0.

The overlap between the Majorana fermions through the TS region gives rise to a finite constant level splitting, the E_0 term, which is independent of f and $\delta\varphi$. Note that such a constant term is missing in the former case where the overlap happens in the NS region. This is attributed to the topological difference between subgap states in TS and NS regions: The pseudospin directions of the two subgap states ($\nu = 1,2$) in the TS region are parallel to each other (see Fig. 5). Technically, the coefficients in Eqs. (A3) and (A4) in the TS region do not depend on the phases f and $\delta\varphi$. The constant splitting E_0 increases as the TS segment length decreases, eventually reaching the band gap $E_{\rm gap}$ at $L_T \to 0$. Because of this constant splitting, no crossing between the subgap states at the Fermi level takes place.

The phase-dependent term, the E_C term, is identical to that of a SQUID made of two normal Josephson junctions threaded by a magnetic flux f, in which the phase differences in the two junctions are $\delta\varphi$ and $4\pi f - \delta\varphi$, respectively. The E_C term can be directly inferred by substituting the superconducting phases in Eq. (3) according to the same rule, Eq. (28), as used in the

short-NS-segment case:

$$E_C\,[\cos(\varphi_L-\varphi_M)+\cos(\varphi_M-\varphi_R)] \\ \rightarrow\; E_C\,[\cos\delta\varphi+\cos(4\pi f-\delta\varphi)]\,. \tag{34}$$

This dependence on $\delta\varphi$ and f confirms our prediction discussed in Sec. I that it is a Cooper pair that tunnels through the NS-TS junctions if the Majorana fermions are coupled via the NS region [see Fig. 2(b)]. The overlap between Majorana fermions opens a channel at $E_A \neq 0$. The Cooper pair then circulates around the loop via the successive Andreev reflection in each junction. Hence the periodicity of the subgap energy E_A with respect to the magnetic flux f is 1/2 as can be seen in Fig. 6(e). Note that the Rashba phase does not affect the E_C term since it gives rise to a phase $4\pi\times 1/2 = 2\pi$. Namely, the Rashba phase acquired by a Cooper pair is twice larger than that by a single electron.

By using Eqs. (22), (23), and (32), the corresponding supercurrent is obtained as [34]

$$I \approx (1-2d^\dagger d)\frac{2e}{\hbar}E_C\,[\sin\delta\varphi+\sin(\delta\varphi-4\pi f)] \\ =(1-2d^\dagger d)\frac{4e}{\hbar}E_C\cos 2\pi f\,\sin(\delta\varphi-2\pi f). \tag{35}$$

The above expression clearly shows the f=1/2 periodicity. By comparing Eq. (31) and (35), one can notice that while in both CAR and NAR processes the magnetic flux f shifts the current by $2\pi f$, it also modulates clearly the amplitude of the current in the NAR process with the weighting factor $\cos 2\pi f$. Hence, apart from the periodicity with respect to f, the modulation of the current can be used to distinguish the CAR process due to the Majorana fermions from the ordinary NAR process. Also, the current due to the NAR, proportional to E_C, is usually smaller than that from the CAR since the Cooper pair tunneling, via the NAR, is a higher order process: Note that the E_M and E_Z terms originate from a single electron circulation around the loop.

C. Small loops ($L_N \sim \lambda_{N1}$, $L_T \sim \lambda_{T1}$)

Up to now, we have considered the cases in which the loop is large enough that only one of CAR and NAR processes is operative. However, if the loop is small or the localization length of the Majorana fermion is comparable to the circumference of the loop, both processes can coexist. The general form of the subgap energy is then given by

$$E_A \approx E_0 + E_C\,[\cos\delta\varphi+\cos(4\pi f-\delta\varphi)] \\ +E_M\cos(2\pi f+\gamma_M)+E_Z\cos(\delta\varphi-2\pi f+\gamma_Z). \tag{36}$$

In Fig. 8 we present the subgap energy in the case where both L_N and L_T are comparable to the Majorana fermion size, $L_N/\lambda_{N1} \sim L_T/\lambda_{T1} \sim 2$. In this case we have obtained

$$\frac{E_0}{E_{\rm gap}}\approx 0.30,\quad \frac{E_C}{E_{\rm gap}}\approx -0.02, \\ \frac{E_M}{E_{\rm gap}}\approx 0.13,\quad \frac{E_Z}{E_{\rm gap}}\approx 0.12,\quad \gamma_M\approx -0.23,\quad \gamma_Z\approx 0.$$

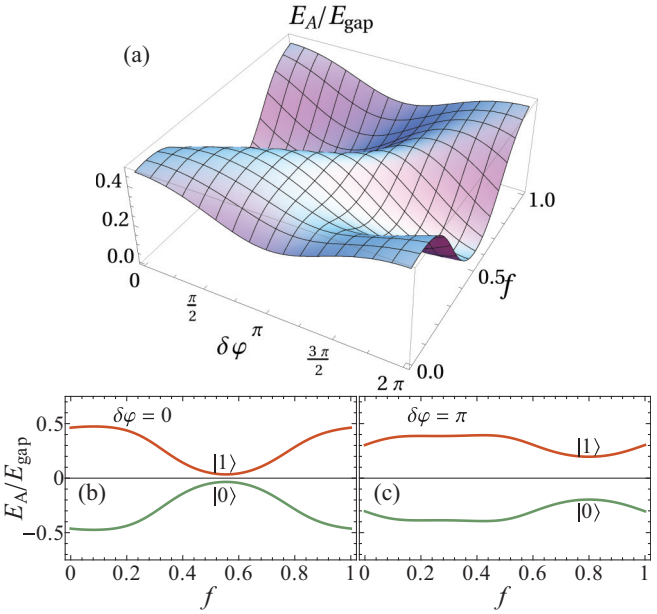

FIG. 8. (Color online) (a) Subgap energy for the state $|1\rangle$ as a function of $\delta\varphi$ and f for a loop with short NS and short TS segments: $L_N/\lambda_{N1}\approx 1.84$ and $L_T/\lambda_{T1}\approx 1.81$. (b) Subgap energies for states $|1\rangle$ and $|0\rangle$ as functions of f at fixed values of $\delta\varphi$. Here we have used $\tilde{\Delta}=3$, $\tilde{\mu}_N=-2$, $\tilde{\mu}_T=1.3$, and $E_{\rm gap}\approx 25\ \mu$eV.

While the E_C term is still small due to its nature of high-order processes, the other terms are comparable. Since the E_C term is negligible, the supercurrent through the loop is almost due to the CAR process. The most intriguing point here is that the $f=1$ periodicity is protected even if there is fermion parity breaking such as coupling to gapless metal or finite-temperature inelastic processes. Figure 8(b) and 8(c) show that there is no crossing between $|0\rangle$ and $|1\rangle$ states. The constant E_0 term, larger than the other terms, makes a big energy separation between $|0\rangle$ and $|1\rangle$ states so that they are not coupled even if there is fermion parity breaking. This kind of protection of $f=1$ periodicity was also noticed in Ref. [25]. In our system, this protection not only guarantees observing the $f=1$ periodicity but also provides us with a way to observe the perfect CAR process without other deterioration.

IV. POSSIBLE EXPERIMENT

In Sec. II and Fig. 3, we have assumed an idealistic setup of a circular ring in close proximity to bulk superconductors with external magnetic field perpendicular to the plane of the ring and with locally tunable gates. In realistic experiments, the setup can be modified without changing the essential, qualitative features of our findings concerning the topologically nontrivial roles of the localized Majorana fermions. Here we briefly discuss possible modifications.

First of all, the ring need not be a perfect circle as long as the nanowire forms a closed loop. While some semiconducting materials grow in a ring shape [29], there is no report of growing InSb or InAs nanowires in a ring. Experimental realization may prefer, for example, a rectangular shape (see Fig. 9) with straight semiconductor segments (instead of curved segments) in favor of easier layering of nanowires and superconductors.

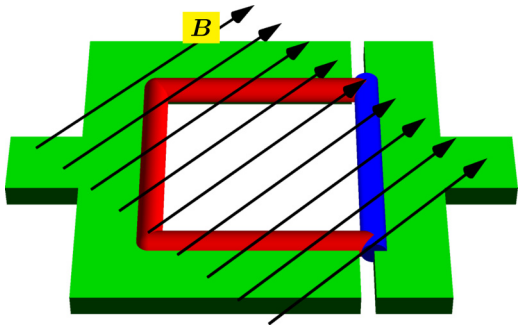

FIG. 9. (Color online) A modified setup for more realistic experimental realization. The nanowire forms a rectangular loop with straight segments (instead of curved ones). The uniform magnetic field in plane, avoiding the shielding by the superconductors, has everywhere a finite component locally perpendicular to the effective Rashba field. The bulk superconductors cover only half of the nanowire hence allowing us to tune locally the chemical potential of the nanowire.

Second, usually the Meissner effect of the bulk superconductors makes it difficult to apply magnetic field on the nanowire perpendicular to the plane. However, the recent experiment [17] demonstrates that by letting the superconductor cover only half of the nanowire, it is possible to apply magnetic field in any direction. Further, the magnetic field can also be applied in-plane as long as it has everywhere a finite component locally perpendicular to the effective Rashba field (which is perpendicular to the nanowire and parallel to the plane). One possible way is to apply a circularly rotating magnetic field generated by an external current along a straight line threading through the plane. When the nanowire has a rectangular shape, it is sufficient to apply a uniform magnetic field in the diagonal direction as depicted in Fig. 9.

Third, the electrical screening by bulk superconductors makes it hard to tune locally the chemical potential of the nanowire. This was overcome by again covering only half of the nanowire with the superconductor in Ref. [17] and by suspending the nanowire segment in question over the conducting silicon substrate in Ref. [19].

Finally, in order to prove our claim that the rectangular loop depicted in Fig. 9 exhibits qualitatively the same transport features as the circular loop does, we have built up a tight-binding model and numerically obtained the subgap state energy for the rectangular loop under the in-plane Zeeman field: refer the detailed description of the tight-binding model to Appendix D. Figure 10 demonstrates that the dependence of the subgap state energy on f and $\delta\varphi$ in two extreme cases—short NS [Fig. 10(a)] and short TS cases [Fig. 10(b)]—for the rectangular loop is qualitatively identical to that for the circular loop under the out-of-plane Zeeman field [see Figs. 6(a) and 6(d)]: First of all, the periodicity on f is 1 and 1/2 for the short NS and short TS cases, respectively, identical to the circular loop, which proves the appearance of the anomalous CAR in the short NS case. A finite constant level splitting is also observed in the short TS case. Small deformations of the curves, which are not essential, are attributed to the partial reflection of the propagating modes at the sharp corners and the resultant modification of interference between the modes. The only nontrivial difference between the effects by the

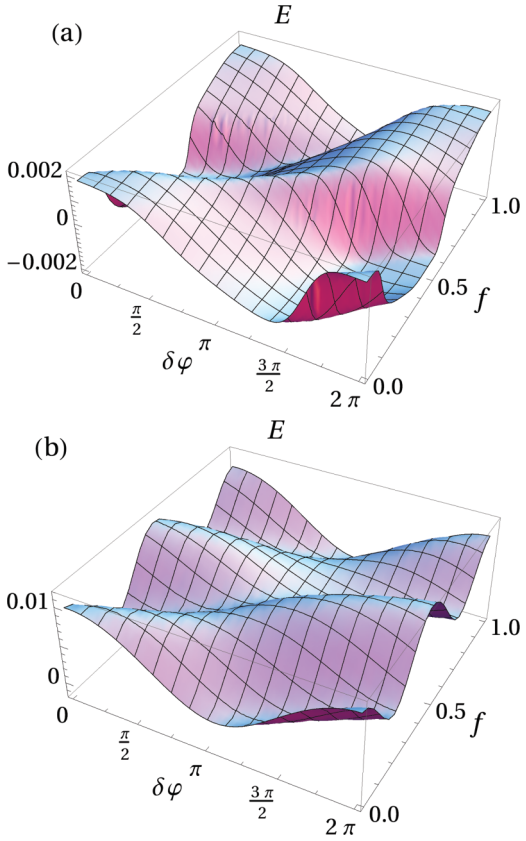

FIG. 10. (Color online) Subgap energy for the state $|1\rangle$ as a function of $\delta\varphi$ and f, obtained from the tight-binding model (see Appendix D) for the setup depicted in Fig. 9. Panels (a) and (b) correspond to a loop with short NS and long TS segments ($N_N = 20$ and $N_T = 180$) and a loop with long NS and short TS segments ($N_N = 90$ and $N_T = 10$), respectively. Here we have used $t = 1$, $t_R = 0.1$, $\mu_N = 0.05$, $\mu_T = 0$, $V_Z = 0.08$, and $\Delta = 0.03$. Refer the definition of tight-binding model parameters to Appendix D.

out-of-plane and in-plane Zeeman splittings is that the sign of E_C is negative in the former case while it is positive in the latter case: Compare Fig. 6(d) and Fig. 10(b). The sign change is attributed to the additional spin rotation by the in-plane Zeeman splitting: Note that an electron, as it goes around the loop, feels the effective rotation of the in-plane Zeeman field, which adds an additional phase π to $\delta\varphi$ in the short TS case. This additional phase does not appear in the anomalous CAR since the two electrons rotate in the opposite directions so that the phase by the spin rotation is canceled out.

V. CONCLUSION

We have considered a system of TS-NS double junctions in loop geometry to investigate its supercurrent characteristics associated with the underlying topological properties and Majorana subgap states localized at the junctions. The system allows us to study on an equal footing TS-NS-TS and NS-TS-NS double junctions, which turn out to have topologically distinct supercurrent characteristics. In this setup, the relative phases across the junctions are controlled by the Aharonov-Bohm phase from the threading magnetic flux as well as the

phase difference between bulk the superconductors that induce the p-wave superconductivity in the nanowire.

We have found that TS-NS-TS and NS-TS-NS double junctions, seemingly counterparts of each other, have substantially different supercurrent characteristics due to the topological properties of their subgap states. In our ring geometry containing both types of double junction, the supercurrent characteristics depend strongly on the ratios of the wire segment lengths and the localization lengths of the Majorana states. For short (compared with the localization lengths of the Majorana states) NS and long TS segment (Sec. III A), the supercurrent originates solely from the crossed Andreev reflection, exhibiting an unusual dependence on the magnetic flux. For short TS and long NS segment (Sec. III B), on the contrary, the normal Andreev reflection (NAR) determines the supercurrent, whose sign can be oscillatory with the TS segment length. The difference in the supercurrent features of the two extreme cases is explained in terms of topological properties in the subgap states (Sec. II C). The representative characteristics in the above two extreme cases compete with each other and show rich effects, which we study by varying the lengths of NS and TS segment (Sec. III C). Finally, the anomalous CAR effect is found to manifest itself in (i) $f = 1$ periodicity of the supercurrent and (ii) the immunity of the supercurrent amplitude to the magnetic flux f. The $f = 1$ periodicity can be robust against, if any, the fermion-parity breaking processes as long as the loop is small enough that the Majorana fermions are coupled through both the NS and TS segments.

ACKNOWLEDGMENTS

This work was supported by National Research Foundation of Korea (NRF) grants funded by the Korean government (MSIP) (No. 2011-0030046, No. 2011-0012494, and No. 2010-0025880).

APPENDIX A: PERTURBATIVE APPROACH

In order to obtain an analytical expression for the subgap energy E_A as a function of $\delta\varphi$ and f, we take a perturbative approach, performing a similar calculation used in Refs. [23] and [25]. First we neglect the interaction between two Majorana states, each of which is localized at the interface, through the TS and NS regions. In our ring geometry, it is done by applying the boundary conditions only at one of the boundaries; see Eq. (20). Suppose that $\Psi_a(x)$ and $\Psi_b(x)$ are the unperturbed Majorana wave functions localized at $x = x_a$ and $x = b$, respectively. Then, $\Psi_b(x)$ is the zero-energy eigenstate of the Hamiltonian, Eq. (11) in the region $0 < x < L$ including the boundary $x = x_b$, but not $x = x_a$. Therefore, $\Psi_b(x)$ satisfies the boundary condition at $x = b$ only. Similarly, $\Psi_a(x)$ is defined in the region $L_N < x < L + L_N$ and satisfies the boundary conditions at $x = x_a$ only. The wave functions are then given by linear combinations of the zero-energy eigenstates in Eq. (17), whose coefficients are determined via the boundary conditions, Eq. (20). Explicitly, the normalized wave functions for $\Psi_i(x)$ $(i = a,b)$ are

$$\Psi_i(x) = \begin{cases} \Psi_{iN}(x), & x_a < x < x_b, \\ \Psi_{iT}(x), & x_b < x < L, \end{cases} \tag{A1}$$

with

$$\Psi_{aN}(x) = \sum_\nu \frac{c_{aN\nu}}{\sqrt{N_a}} \chi^N_{+,\nu}(x), \tag{A2a}$$

$$\Psi_{aT}(x) = \sum_\nu \frac{c_{aT\nu}}{\sqrt{N_a}} e^{(i\nu k_r - 1/\lambda_{N\nu})L} \chi^T_{-,\nu}(x), \tag{A2b}$$

$$\Psi_{bN}(x) = \sum_\nu \frac{c_{bN\nu}}{\sqrt{N_b}} e^{-L_N/\lambda_{N\nu}} \chi^N_{-,\nu}(x), \tag{A2c}$$

$$\Psi_{bT}(x) = \sum_\nu \frac{c_{bT\nu}}{\sqrt{N_b}} e^{-(i\nu k_r - 1/\lambda_{N\nu})L_N} \chi^T_{+,\nu}(x). \tag{A2d}$$

Note here that the additional exponential factors have been inserted to make the coefficients of order 1 at the localization center. The coefficients are

$$c_{aN1} = \frac{\sin[\gamma - 2\pi(f + 1/2) + \delta\varphi/2]}{\sin\gamma}, \tag{A3a}$$

$$c_{aN2} = e^{i\gamma} \frac{\sin[2\pi(f + 1/2) - \delta\varphi/2]}{\sin\gamma}, \tag{A3b}$$

$$c_{aT1} = \frac{1}{2}\left(1 + \sqrt{\frac{D - \tilde{\mu}_N}{D - \tilde{\mu}_T}}\right), \tag{A3c}$$

$$c_{aT2} = \frac{1}{2}\left(1 - \sqrt{\frac{D - \tilde{\mu}_N}{D - \tilde{\mu}_T}}\right), \tag{A3d}$$

and

$$c_{bN1} = \frac{\sin(\gamma - \delta\varphi/2)}{\sin\gamma}, \tag{A4a}$$

$$c_{bN2} = e^{-i\gamma} \frac{\sin(\delta\varphi/2)}{\sin\gamma}, \tag{A4b}$$

$$c_{bT1} = \frac{1}{2}\left(1 + \sqrt{\frac{D - \tilde{\mu}_N}{D - \tilde{\mu}_T}}\right), \tag{A4c}$$

$$c_{bT2} = \frac{1}{2}\left(1 - \sqrt{\frac{D - \tilde{\mu}_N}{D - \tilde{\mu}_T}}\right). \tag{A4d}$$

The normalization constants are given by

$$N_i = \frac{1}{R}\sum_\nu \left[\frac{|c_{iN\nu}|^2}{\lambda^{-1}_{N\nu}} + 2\cos\gamma \frac{|c_{iN\nu} c_{iN\bar{\nu}}|}{\lambda^{-1}_{N1} + \lambda^{-1}_{N2}} + \frac{|c_{iT\nu}|^2}{\lambda^{-1}_{T\nu}} + \frac{2c^*_{iT\nu} c_{iT\bar{\nu}}}{2(-1)^\nu i k_r + \lambda^{-1}_{T1} + \lambda^{-1}_{T2}} \right]. \tag{A5}$$

Here the normalization constants are obtained up to the leading order in the small factor $e^{-L/\lambda_{\ell\nu}}$, which is consistent with our perturbation. Note that the Rashba phase appears explicitly in the coefficients $c_{aN\nu}$ in the form of $f + 1/2$, as discussed in Sec. II B.

The effective Hamiltonian projected to the Majorana subspace is then represented as

$$H_{\rm M} = \begin{bmatrix} \langle\Psi_a|H^{\rm BdG}_{\rm eff}|\Psi_a\rangle & \langle\Psi_a|H^{\rm BdG}_{\rm eff}|\Psi_b\rangle \\ \langle\Psi_b|H^{\rm BdG}_{\rm eff}|\Psi_a\rangle & \langle\Psi_b|H^{\rm BdG}_{\rm eff}|\Psi_b\rangle \end{bmatrix}. \tag{A6}$$

Since $\Psi_i(x)$ are not the eigenstates of the full Hamiltonian $H_{\rm eff}^{\rm BdG}$, the diagonal terms does not vanish. However, we ignore them since they are proportional to the square of the exponential factor $e^{-L/\lambda_{\ell\nu}}$ and much smaller than the off-diagonal terms. The formal expression for the off-diagonal terms are

$$H_{M,ab} = i\{\Psi_a^\dagger(x_a)[v_\phi\Psi_b(x_a^-) - v_\phi\Psi_b(x_a^+)] + [v_\phi\Psi_a(x_a)]^\dagger[\Psi_b(x_a^-) - \Psi_b(x_a^+)]\}, \quad \text{(A7a)}$$

$$H_{M,ba} = -i\{\Psi_b^\dagger(x_b)[v_\phi\Psi_a(x_b^+) - v_\phi\Psi_a(x_b^-)] + [v_\phi\Psi_b(x_b)]^\dagger[\Psi_a(x_b^+) - \Psi_a(x_b^-)]\}. \quad \text{(A7b)}$$

Since $\Psi_a(x)$ and $\Psi_b(x)$ are not orthogonal to each other, the effective Hamiltonian is not necessarily Hermitian, $H_{M,ab} \neq H_{M,ba}^*$. The subgap energy is then obtained as

$$E_A = \pm\sqrt{H_{M,ab}H_{M,ba}}. \quad \text{(A8)}$$

Explicit and tedious calculations lead to

$$H_{M,ab} = +iE_R\frac{e^{-i\gamma}}{\sqrt{N_aN_b}}\sum_{\ell\nu} e^{-L_\ell/\lambda_{\ell\nu}}h_{\ell\nu}^-, \quad \text{(A9a)}$$

$$H_{M,ba} = -iE_R\frac{e^{+i\gamma}}{\sqrt{N_aN_b}}\sum_{\ell\nu} e^{-L_\ell/\lambda_{\ell\nu}}h_{\ell\nu}^+, \quad \text{(A9b)}$$

with

$$h_{N\nu}^\pm = \frac{(-1)^\nu\epsilon_1}{\sin\gamma}[\cos(2\pi f+\gamma'-\zeta_\nu) - \cos(\delta\varphi-2\pi f\pm\gamma')] \quad \text{(A10)}$$

with $\zeta_1 = 2\gamma$ and $\zeta_2 = 0$ and

$$h_{T\nu}^\pm = \epsilon_1\sin(\gamma-\gamma') - (-1)^\nu(\epsilon_2\sin\gamma - \epsilon_3\cos\gamma) \quad \text{(A11)}$$

for $0 < \tilde{\mu}_T < D$ and

$$\sum_\nu h_{T\nu}^\pm = 2\epsilon_1\sin(\gamma-\gamma')\cos k_rL_T + 2(\epsilon_2\sin\gamma - \epsilon_3\cos\gamma)\sin k_rL_T \quad \text{(A12)}$$

for $D < \tilde{\mu}_T$. Here we have defined

$$\epsilon_1 \equiv \sqrt{\tilde{\Delta}^2 - 4\tilde{\mu}_N}, \quad \text{(A13a)}$$

$$\epsilon_2 \equiv \frac{2D-\tilde{\mu}_N-\tilde{\mu}_T}{\sqrt{|D-\tilde{\mu}_T|}}, \quad \text{(A13b)}$$

$$\epsilon_3 \equiv \frac{\sqrt{D-\tilde{\mu}_N}}{\sqrt{|D-\tilde{\mu}_T|}}, \quad \text{(A13c)}$$

and

$$\cos\gamma' \equiv \sqrt{1-1/\epsilon_1^2}, \quad \sin\gamma' \equiv 1/\epsilon_1. \quad \text{(A14)}$$

In the large-curvature limit ($R\to\infty$) where $\gamma\to\pi/2$ and $\gamma'\to 0$, the coefficients are simplified to

$$h_{N\nu}^\pm = \epsilon_1[\cos 2\pi f - (-1)^\nu\cos(\delta\varphi - 2\pi f)], \quad \text{(A15a)}$$

$$h_{T\nu}^\pm = \epsilon_1 - (-1)^\nu\epsilon_2 \quad (\tilde{\mu}_T < D), \quad \text{(A15b)}$$

$$\sum_\nu h_{T\nu}^\pm = 2\epsilon_1\cos k_rL_T + 2\epsilon_2\sin k_rL_T \quad (\tilde{\mu}_T > D), \quad \text{(A15c)}$$

and

$$N_a = N_0 + \frac{\sqrt{D}}{-\tilde{\mu}_N}\cos(4\pi f - \delta\varphi), \quad \text{(A16a)}$$

$$N_b = N_0 + \frac{\sqrt{D}}{-\tilde{\mu}_N}\cos\delta\varphi, \quad \text{(A16b)}$$

with

$$N_0 \equiv \frac{\sqrt{D-\tilde{\mu}_N}}{-\tilde{\mu}_N} + \frac{\sqrt{D}+\sqrt{D-\tilde{\mu}_N}}{\tilde{\mu}_T} + \frac{\tilde{\mu}_T-\tilde{\mu}_N}{2\tilde{\mu}_T\sqrt{D}}, \quad \text{(A17)}$$

where N_0 is the value of the normalization constants $N_{a,b}$ averaged over the phases.

APPENDIX B: FINITE-CURVATURE EFFECT ON PHASE SHIFTS

In our main calculation, we have used the ring geometry for simplicity. Due to the finite curvature of the ring, the clockwise and counterclockwise movers experience opposite spin rotation along the z direction, introducing asymmetry between them. The asymmetry enters into the subgap energy, Eq. (26), in terms of the phase shifts, γ_M and γ_Z, in the E_M and E_Z terms, respectively.

Our numerical calculations find that the phase γ_Z is found to be almost zero, irrespective of the segment length, as can be seen in Fig. 11. This implies that the curvature of the loop does not affect the transport due to the CAR process.

In contrast, the phase γ_M is finite; see Fig. 11. In the case of $L_N > \lambda_{N1}$ and $L_T > \lambda_{T1}$, where the perturbation is valid, the phase is given by $\pi - 2\gamma$ which is the phase shift for the $\nu = 1$ mode for $\gamma' \approx 0$ [see Eq. (A10)]. For $L_N < \lambda_{N1}$, both $\nu = 1,2$ modes are contributing so that the phase γ_M becomes length dependent. The phase γ_M becomes negligible only when the size of the loop is sufficiently large: in this case $\tilde{\Delta} \gg 1$ and $\gamma \approx \pi/2$ [see Eq. (19)]. The phase shift γ_M comes from the finite curvature of the ring and the resultant phase shift of the

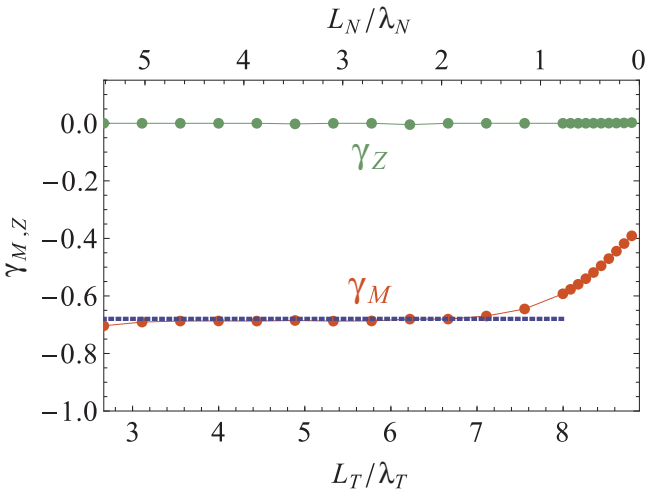

FIG. 11. (Color online) The phase shifts γ_M and γ_Z as functions of L_N or $L_T = L - L_N$ with $L = L_N + L_T$ fixed. The same values of parameters as in Fig. 7 are used. The dotted line refers to the perturbative result, $\pi - 2\gamma$.

Majorana states. Our results show that this phase appears only in the E_M term, not in the E_Z term and, more importantly, not in E_C term, either. Hence, the existence of the finite phase shift γ_M can be used for the evidence of the Majorana fermions as well.

APPENDIX C: OSCILLATORY BEHAVIOR IN SUBGAP ENERGY COEFFICIENTS E_0 AND E_C IN DEEP TOPOLOGICAL PHASE

In the main text, we have focused on the $\tilde{\mu}_T < D$ case such that the zero-energy solutions $k^T_{\eta\mu}$ of Eq. (12) in the TS region are purely imaginary. However, when the TS region is in the deep topological phase ($\tilde{\mu}_T > D$), the wave vectors $k^T_{\eta\mu}$ have real parts:

$$k^T_{\eta\nu} = \eta[(-1)^\nu k_r + i/\lambda_{T\nu}] \tag{C1}$$

with the real and imaginary parts are given by

$$k_r = \frac{\sqrt{\tilde{\mu}_T - D}}{R}, \quad \lambda_{T\nu} = \frac{R}{\sqrt{D}}. \tag{C2}$$

The finite real part adds the oscillatory nature to the Majorana wave function in the TS region. Hence, it can become effective if the overlap between Majorana states in the TS region is nontrivial. So, we consider the case in which the TS segment is short and the NS segment long as in Sec. III B. The empirical expression for the subgap energy is the same as Eq. (32) except that the coefficients are now approximated by

$$E_0 \approx \frac{E_R}{N_0} 2e^{-L_T/\lambda_{T1}} (\epsilon_1 \cos k_r L_T + \epsilon_2 \sin k_r L_T), \tag{C3a}$$

$$E_C \approx \frac{\sqrt{D}}{2\tilde{\mu}_N N_0} E_0. \tag{C3b}$$

While the E_0 and E_C terms [see Eqs. (33a) and (33b)] in the weak topological phase ($\tilde{\mu}_T < D$) are monotonically decreasing with increasing L_T, the coefficients in the deep topological phase are, apart from the exponentially decreasing envelop part, oscillatory with $k_r L_T$. This is surely owing to the oscillatory behavior of the Majorana wave function in the deep topological phase due to the finite real part of the wave vectors, k_r [see Eq. (C2)]. Figure 12 demonstrates the sign-changing oscillatory behavior of the coefficients E_0 and E_C. In the deep topological regime (marked by A and B), E_0 and E_C exhibit oscillations whose period is identified by $2\pi/k_r$ as expected from the sinusoidal dependence in Eq. (C3a). In the weak topological regime (marked by C), no oscillation is observed and the monotonic dependence of the coefficients E_0 and E_C on L_T is observed. Note that the sign of the supercurrent can be controlled not only by tuning the TS segment length L_T but also by changing the period $2\pi/k_r$. The latter control can be done by tuning the chemical potential $\tilde{\mu}_T$ [see Eq. (C2)]. This oscillatory feature is peculiar in that it cannot be observed in the usual normal superconductor SQUID hosting no Majorana fermions. Majorana-based SQUID then provides an electronic way to change the sign of the supercurrent.

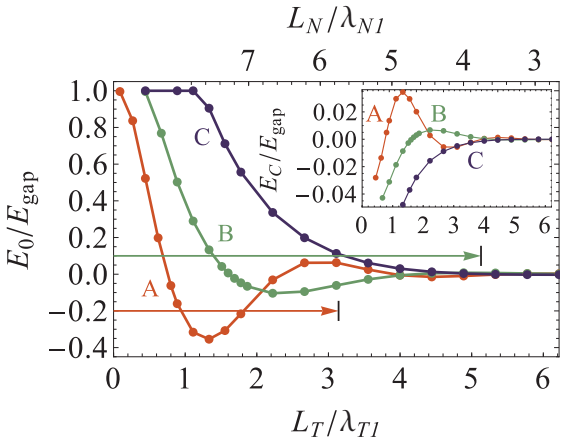

FIG. 12. (Color online) The coefficients E_0 and E_C (inset) as functions of L_N or $L_T = L - L_N$ with $L = L_N + L_T$ fixed. The parameters used are $\tilde{\Delta} = 3$, $\tilde{\mu}_N = -5$, and $\tilde{\mu}_T = 10$ (deeper topological phase) [marked by A], 5 (deep topological phase) [marked by B], and 2.5 (weak topological phase) [marked by C]. The arrows indicate the oscillation periods, $2\pi/k_r$ for the cases A and B.

APPENDIX D: TIGHT-BINDING MODEL FOR RECTANGULAR LOOP

In Sec. IV, we have introduced a more realistic experimental realization which forms a rectangular loop as seen in Fig. 9. The continuous model used in Sec. II for the ring-shaped loop is rather inadequate for the rectangular loop due to the difficulty to treat its sharp corners properly. This is the reason why we have chosen the idealistic circular loop for our main target: the simple wave-function-matching method is applicable and the (perturbative) analytical expression is at hands. For the study of the rectangular loop, instead, we use a numerical method based on a tight-binding model; see Fig. 13. Following the standard procedure to build up a tight-binding model [30], the

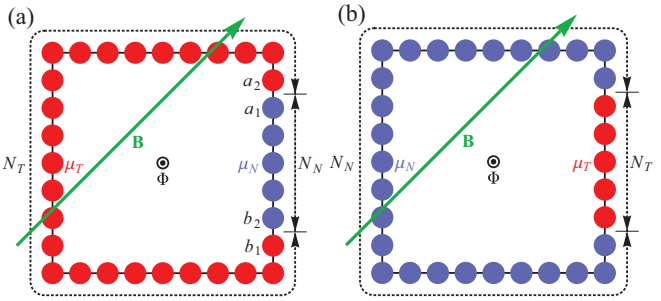

FIG. 13. (Color online) Illustration of a tight-binding model for the cases of (a) short NS and long TS segments and (b) long NS and short TS segments. Each segment consists of N_N (NS, blue) and N_T (TS, red) sites and is under the chemical potential μ_N and μ_T. Uniform in-plane magnetic field **B** is applied in the direction indicated by the arrow in order to induce p-wave superconductivity. Small perpendicular magnetic field, which is smaller than the critical field for superconductor, gives rise to the magnetic flux $\Phi = f\Phi_0$ enclosed by the loop.

Schrödinger equation is given by

$$E\Psi_i = \sum_j H_{ij}\Psi_j, \tag{D1}$$

where

$$\Psi_i = \begin{bmatrix} u_{i\uparrow} \\ u_{i\downarrow} \\ v_{i\downarrow} \\ v_{i\uparrow} \end{bmatrix} \tag{D2}$$

is the wave function at site i in the Nambu space. The Hamiltonian element in the absence of the magnetic flux ($f = 0$) and the superconducting phase difference ($\delta\varphi = 0$) is obtained as

$$H_{ij} = \delta_{i,j}\left[(2t - \mu_i)\tau_z + \frac{V_Z}{2}\frac{\sigma_x + \sigma_y}{\sqrt{2}}\tau_z - \Delta\tau_x\sigma_z\right] + \delta_{i+1,j}[-t\tau_z - it_R\boldsymbol{\sigma}\cdot\mathbf{u}_{ij}] + \delta_{i-1.j}[-t\tau_z + it_R\boldsymbol{\sigma}\cdot\mathbf{u}_{ij}]. \tag{D3}$$

Here $\tau_{x,y,z}$ are the Pauli matrices in the Nambu space, t the hopping amplitude, μ_i the position-dependent chemical potential, V_Z the Zeeman splitting due to the in-plane magnetic field, Δ the superconducting gap, t_R the Rashba spin-orbit coupling strength, and $\mathbf{u}_{ij}$ the unit vector parallel to the Rashba field at the link connecting sites i and j. As shown in Fig. 13, the numbers of the sites of NS and TS segments are N_N and N_T, respectively. Two segments are distinguished by imposing different chemical potentials, μ_N and μ_T, respectively. In the presence of the magnetic flux and the phase difference, the off-diagonal elements $H_{i\neq j}$ acquire additional phases. Applying a proper gauge transformation, one can make the finite phases appear only at the junctions between two segments:

$$H_{ij} = e^{-i\tau_z\alpha_{j,i}}H_{ij}(f = 0, \delta\varphi = 0) \tag{D4}$$

with

$$\alpha_{j,i} = -\alpha_{i,j} = \begin{cases} \frac{\delta\varphi}{2}, & (i,j) = (a_1,a_2), \\ 2\pi f - \frac{\delta\varphi}{2}, & (i,j) = (b_1,b_2), \\ 0, & \text{otherwise.} \end{cases} \tag{D5}$$

See Fig. 13(a) for the location of sites $a_{1,2}$ and $b_{1,2}$. Numerical diagonalization of the Schrödinger equation, Eq. (D1), directly gives rise to the energy of the subgap states localized at the junctions.

[1] P. A. M. Dirac, Proc. R. Soc. London A **117**, 610 (1928).
[2] P. A. M. Dirac, Proc. R. Soc. London A **126**, 360 (1930).
[3] E. Majorana, Nuovo Cimento **14**, 171 (1937).
[4] A. Yu. Kitaev, Ann. Phys. **303**, 2 (2003).
[5] S. Das Sarma, M. Freedman, and C. Nayak, Phys. Today **59**(7), 32 (2006).
[6] C. Nayak, S. H. Simon, A. Stern, M. Freedman, and S. Das Sarma, Rev. Mod. Phys. **80**, 1083 (2008).
[7] F. Wilczek, Nat. Phys. **5**, 614 (2009).
[8] M. Franz, Physics **3**, 24 (2010).
[9] A. Yu Kitaev, Phys.-Usp. **44**, 131 (2001).
[10] J. D. Sau, R. M. Lutchyn, S. Tewari, and S. Das Sarma, Phys. Rev. Lett. **104**, 040502 (2010).
[11] R. M. Lutchyn, J. D. Sau, and S. Das Sarma, Phys. Rev. Lett. **105**, 077001 (2010).
[12] J. Alicea, Phys. Rev. B **81**, 125318 (2010).
[13] Y. Oreg, G. Refael, and F. von Oppen, Phys. Rev. Lett. **105**, 177002 (2010).
[14] J. Alicea, Y. Oreg, G. Refael, F. von Oppen, and M. P. A. Fisher, Nat. Phys. **7**, 412 (2011).
[15] J. Alicea, Rep. Prog. Phys. **75**, 076501 (2012).
[16] C. W. J. Beenakker, Annu. Rev. Condens. Matter Phys. **4**, 113 (2013).
[17] V. Mourik, K. Zuo, S. M. Frolov, S. R. Plissard, E. P. A. M. Bakkers, and L. P. Kouwenhoven, Science **336**, 1003 (2012).
[18] M. T. Deng, C. L. Yu, G. Y. Huang, M. Larsson, P. Caroff, and H. Q. Xu, Nano Letters **12**, 6414 (2012).
[19] A. Das, Y. Ronen, Y. Most, Y. Oreg, M. Heiblum, and H. Shtrikman, Nat. Phys. **8**, 12 (2012).
[20] J. Liu, A. C. Potter, K. T. Law, and P. A. Lee, Phys. Rev. Lett. **109**, 267002 (2012).
[21] F. Pientka, G. Kells, A. Romito, P. W. Brouwer, and F. von Oppen, Phys. Rev. Lett. **109**, 227006 (2012).
[22] D. Rainis, L. Trifunovic, J. Klinovaja, and D. Loss, Phys. Rev. B **87**, 024515 (2013).
[23] L. Jiang, D. Pekker, J. Alicea, G. Refael, Y. Oreg, and F. von Oppen, Phys. Rev. Lett. **107**, 236401 (2011).
[24] B. van Heck, A. R. Akhmerov, F. Hassler, M. Burrello, and C. W. J. Beenakker, New J. Phys. **14**, 035019 (2012).
[25] F. Pientka, A. Romito, M. Duckheim, Y. Oreg, and F. von Oppen, New J. Phys. **15**, 025001 (2013).
[26] L. Fu and C. L. Kane, Phys. Rev. B **79**, 161408(R) (2009).
[27] S.-Q. Shen, *Topological Insulators*, Vol. 174 of Springer Series in Solid-State Sciences (Springer, Berlin, 2012).
[28] J. Splettstoesser, M. Governale, and U. Zülicke, Phys. Rev. B **68**, 165341 (2003).
[29] P. J. Pauzauskie, D. J. Sirbuly, and P. Yang, Phys. Rev. Lett. **96**, 143903 (2006).
[30] S. Datta, *Electronic Transport in Mesoscopic Systems* (Cambridge University Press, Cambridge, 1995).
[31] In the closed loop geometry, the applied magnetic flux $f \neq 0$ adds additional relative rotation between the polarization axes at two ends of the same region.
[32] For the supercurrent, in general, one has to calculate all the states including the (almost) continuum of the bulk states. In our study we focus on the contribution from the subgap states.
[33] The supercurrent obtained numerically is not exactly sinusoidal since it includes the contribution from higher order processes. In fact, the coefficients E_Z and E_M are also functions of $\delta\varphi$ through the normalization constants N_a and N_b (see Appendix A).
[34] The approximate expression, Eq. (35), shows some discrepancies from the numerically exact results. For example, the current numerically calculated does not vanish at $f = 1/4$ and $3/4$. It is because the latter includes the contributions from higher order processes.